

# Chemical vapor deposition of superconducting FeTe<sub>1-x</sub>Se<sub>x</sub> nanosheets

Hu, Dianyí; Ye, Chen; Wang, Xiaowei; Zhao, Xiaoxu; Kang, Lixing; Liu, Jiawei; Duan, Ruihuan; Cao, Xun; He, Yanchao; Hu, Junxiong; Li, Shengyao; Zeng, Qingsheng; Deng, Ya; Yin, Peng-Fei; Ariando, Ariando; Huang, Yizhong; Zhang, Hua; Wang, Renshaw Xiao; Liu, Zheng

2021

Hu, D., Ye, C., Wang, X., Zhao, X., Kang, L., Liu, J., Duan, R., Cao, X., He, Y., Hu, J., Li, S., Zeng, Q., Deng, Y., Yin, P., Ariando, A., Huang, Y., Zhang, H., Wang, R. X. & Liu, Z. (2021). Chemical vapor deposition of superconducting FeTe<sub>1-x</sub>Se<sub>x</sub> nanosheets. Nano Letters, 21(12), 5338-5344. <https://dx.doi.org/10.1021/acs.nanolett.1c01577>

<https://hdl.handle.net/10356/151394>

<https://doi.org/10.1021/acs.nanolett.1c01577>

---

This document is the Accepted Manuscript version of a Published Work that appeared in final form in Nano Letters, copyright © American Chemical Society after peer review and technical editing by the publisher. To access the final edited and published work see <https://doi.org/10.1021/acs.nanolett.1c01577>

*Downloaded on 13 Mar 2024 18:17:16 SGT*

# **Realizing Superconductivity in FeTe<sub>1-x</sub>Se<sub>x</sub> Nanosheets**

## **Prepared by Chemical Vapor Deposition**

Dianyi Hu<sup>1</sup>§, Chen Ye<sup>4</sup>§, Xiaowei Wang<sup>1</sup>§, Lixing Kang<sup>1,2</sup>§, Xiaoxu Zhao<sup>1,7</sup>, Jiawei Liu<sup>1</sup>, Ruihuan Duan<sup>1</sup>, Xun Cao<sup>1</sup>, Yanchao He<sup>1</sup>, Junxiong Hu<sup>8</sup>, Peng Meng<sup>1</sup>, Qingsheng Zeng<sup>1</sup>, Ya Deng<sup>1</sup>, Pengfei Yin<sup>5</sup>, Ariando Ariando<sup>8</sup>, Stephen J. Pennycook<sup>7</sup>, Hua Zhang<sup>5,6</sup>, Xiao Renshaw Wang<sup>3,4\*</sup>, Zheng Liu<sup>1,2,3\*</sup>

<sup>1</sup>School of Materials Science and Engineering, Nanyang Technological University, Singapore 639798, Singapore.

<sup>2</sup>CINTRA CNRS/NTU/THALES, UMI 3288, Research Techno Plaza, Singapore 637553, Singapore.

<sup>3</sup>Centre for Micro-/Nano-electronics (NOVITAS), School of Electrical and Electronic Engineering, Nanyang Technological University, Singapore 639798, Singapore.

<sup>4</sup>School of Physical and Mathematical Sciences, Nanyang Technological University, Singapore, 639798, Singapore.

<sup>5</sup>Department of Chemistry, City University of Hong Kong, Kowloon, Hong Kong, China.

<sup>6</sup>Hong Kong Branch of National Precious Metals Material Engineering Research Center (NPMM), City University of Hong Kong, Hong Kong, China.

<sup>7</sup>Department of Materials Science and Engineering, National University of Singapore, Singapore 117575, Singapore.

<sup>8</sup>Department of Physics, National University of Singapore, Singapore, 117551,

Singapore.

§These authors contributed equally: Dianyi Hu, Chen Ye, Xiaowei Wang and Lixing Kang

Correspondence and requests for materials should be addressed to Z.L. (email: z.liu@ntu.edu.sg) and X.R.W. (email: renshaw@ntu.edu.sg)

## **Abstract**

$\text{FeTe}_{1-x}\text{Se}_x$ , a promising material to realize Majorana zero modes (MZMs), has attracted enormous attention in recent years. Pulsed laser deposition (PLD) and molecular-beam epitaxy (MBE) are the routine growth methods to prepare high-quality  $\text{FeTe}_{1-x}\text{Se}_x$  thin films. However, they suffer from high-cost and time-consuming problems, which hinders the exploration of novel two-dimensional (2D) superconductivity and related nanodevices. Here we demonstrate the experimental realization of superconductivity in  $\text{FeTe}_{1-x}\text{Se}_x$  nanosheets prepared by a chemical vapor deposition (CVD) method. The composition and thickness of the 2D  $\text{FeTe}_{1-x}\text{Se}_x$  nanosheets can be controlled by finely tuning the experimental conditions. Further, the as-prepared  $\text{FeTe}_{1-x}\text{Se}_x$  nanosheets exhibit an onset transition temperature of 12.4 K and hold evidence of quasi-2D superconductivity, proving their high quality.

## **Introduction**

Tetragonal  $\text{FeSe}$ , with its simple structure and absence of toxic elements, has attracted

tremendous attention since the discovery of superconductivity with a transition temperature of 8 K in this material.<sup>1-4</sup> Surprisingly, monolayer FeSe film on strontium titanate (STO) substrate was reported to have a superconducting gap corresponding to the superconducting transition temperature ( $T_c$ ) of 86 K, and the  $T_c$  increased to over 100 K when Nb doped-STO was used as the substrate.<sup>5,6</sup> These results show that the Fe-based superconductors are promising candidates to realize high-temperature superconductivity. After doping Te into this material, interesting phenomena have been observed in the  $\text{FeTe}_{1-x}\text{Se}_x$  ternary alloy system. The introduction of heavy Te atoms into the tetragonal FeSe not only stabilizes the structure and dopes the material with electrons, but also brings in strong spin-orbit coupling.<sup>7</sup> Especially, in the case of  $\text{FeTe}_{0.55}\text{Se}_{0.45}$ , non-trivial topology in the band structure has been theoretically predicted, indicating that the  $\text{FeTe}_{0.55}\text{Se}_{0.45}$  may serve as an inherent hybrid system with s-wave superconductivity in the bulk and topological states on the surface, which is also called connate topological superconductor.<sup>7-9</sup> Experimentally, the topological superconductivity and the evidence for Majorana zero modes (MZMs) on the surface of  $\text{FeTe}_{0.55}\text{Se}_{0.45}$  crystal have been observed recently.<sup>10-13</sup> Therefore,  $\text{FeTe}_{1-x}\text{Se}_x$  ternary alloy has been regarded as a promising material to realize MZMs and a potential building block for quantum computing in future.

Compared to  $\text{FeTe}_{1-x}\text{Se}_x$  crystals,  $\text{FeTe}_{1-x}\text{Se}_x$  thin films are more appealing, because they not only have been predicted to realize topological superconductivity at higher temperature than that of the crystals, but also are more suitable for device

intergration.<sup>8,14</sup> Currently, pulsed laser deposition (PLD) and molecular-beam epitaxy (MBE) are the two commonly used methods to prepare  $\text{FeTe}_{1-x}\text{Se}_x$  thin films. However, these methods suffer from several drawbacks. Costly high-vacuum instrumentations are always needed. In addition, only polished crystalline substrates can be used for the growth of ultrathin films.<sup>15</sup> The superconducting properties of these films are usually strongly affected by the substrate arising from lattice mismatch and interface interaction.<sup>15,16</sup> These limit the exploration of the intrinsic superconducting properties of  $\text{FeTe}_{1-x}\text{Se}_x$  thin films.

Chemical vapor deposition (CVD), as a low-cost and powerful method, has been widely applied to prepare a library of 2D materials and their heterostructures in recent years.<sup>17-22</sup> It provides a scalable and controllable way to obtain high-quality and large-area 2D materials. However, superconductivity in  $\text{FeTe}_{1-x}\text{Se}_x$  samples prepared by chemical vapor method has not been reported yet, which may be ascribed to two possible reasons. First, the superconducting coherence length of  $\text{FeTe}_{1-x}\text{Se}_x$  is estimated to be about 3 nm, which makes the superconductivity of this material rather sensitive to defects.<sup>23</sup> This means that its superconductivity can only be unveiled in samples with high quality. Second, excess interstitial Fe atoms in  $\text{FeTe}_{1-x}\text{Se}_x$  can act as localized charge carriers and may induce local magnetic moment, which would decrease the superconducting volume.<sup>24</sup> Thus, a suitable iron precursor should be chosen to ensure better control over the release of reactive Fe precursor. Here, we report the successful realization of superconductivity in tetragonal  $\text{FeTe}_{1-x}\text{Se}_x$  nanosheets prepared by a CVD method on

Si/SiO<sub>2</sub> substrate. The as-prepared FeTe<sub>1-x</sub>Se<sub>x</sub> nanosheets exhibit a rectangular shape with edge length up to 40 μm. By dedicatedly controlling the growth conditions, the thickness of the FeTe<sub>1-x</sub>Se<sub>x</sub> nanosheets can be tuned from a few nanometers to tens of nanometers, and the composition of FeTe<sub>1-x</sub>Se<sub>x</sub> can be tuned from  $x = 0$  to  $x = 0.7$ . The high quality of the prepared samples is confirmed by low-temperature electrical transport measurement. Impressively, the FeTe<sub>1-x</sub>Se<sub>x</sub> sample exhibits an onset superconducting transition temperature of 12.4 K and holds signature of quasi-2D superconductivity, providing a promising platform for the further study of topological superconductivity in FeTe<sub>1-x</sub>Se<sub>x</sub> system.

## Results and Discussion

In a typical experiment, the FeTe<sub>1-x</sub>Se<sub>x</sub> nanosheets are synthesized by using a CVD method at atmospheric pressure. The experimental set-up is illustrated in Figure 1a. A mixture of Fe<sub>2</sub>O<sub>3</sub> and FeCl<sub>2</sub> powders is used as the iron precursor, while Te and Se powders are separately loaded in two quartz boats located at the upstream as the chalcogenide precursors (see the Experimental Section for details). Figure 1b shows the crystal structure of the FeTe<sub>1-x</sub>Se<sub>x</sub> viewed from  $c$  and  $a$  directions, respectively. It consists of a continuous stacking of FeTe<sub>1-x</sub>Se<sub>x</sub> layers in the  $c$  direction and adopts a space group of P4/nmm. In each layer, the square-lattice layer of Fe atoms is sandwiched between two twice-sparsely layers of bonding chalcogen atoms, in which Te and Se atoms are randomly distributed. Figure 1c shows the optical microscopy (OM) image of a typical ultrathin FeTe<sub>1-x</sub>Se<sub>x</sub> nanosheet on the SiO<sub>2</sub>/Si substrate, exhibiting a

rectangular shape with a lateral size as large as 40  $\mu\text{m}$ . The thickness of the ultrathin flake is 3.8 nm measured by atomic force microscopy (AFM) (Figure 1d). To highlight, the products are uniform in thickness, as illustrated in the OM image with larger view (Figure 1e). Several synthetic parameters of our CVD method were studied systematically. It was found that the thickness of the  $\text{FeTe}_{1-x}\text{Se}_x$  nanosheets is positively proportional to the reaction temperature. Figure 1f–h shows the thickness distribution statistics of the nanosheets at the reaction temperature of 500, 520 and 540  $^{\circ}\text{C}$ , respectively, and the insets are the representative OM images of the corresponding products. The optical contrasts of these flakes gradually change from light pink to bright yellow, clearly demonstrating the gradual increase of thickness. In addition, other substrates, including STO(110) and Si(100), can also be used to grow  $\text{FeTe}_{1-x}\text{Se}_x$  nanosheets by our method, but with different morphologies because of the lattice mismatch between different substrates and the  $\text{FeTe}_{1-x}\text{Se}_x$  nanosheets (Figure S1). The direct growth on diverse substrates and the capability to tune the thickness of the obtained nanosheets show the versatility of our synthetic approach and enable us to study the potential interactions between  $\text{FeTe}_{1-x}\text{Se}_x$  and different substrates.

The composition of  $\text{FeTe}_{1-x}\text{Se}_x$  can be controlled by changing the temperatures of Te and Se sources. The temperature of Te source was tuned from 460 $^{\circ}\text{C}$  to 500 $^{\circ}\text{C}$  by changing its location, while the temperature of Se precursor was adjusted from 260 $^{\circ}\text{C}$  to 320 $^{\circ}\text{C}$  by a heating belt. Tuning the temperatures of these two precursors results in a change of the atomic ratio between Te and Se in our sample. The compositional change

of the as-prepared  $\text{FeTe}_{1-x}\text{Se}_x$  is demonstrated by X-ray diffraction (XRD) patterns (Figure 2a). All the characteristic peaks, including (001), (002), (003) and (004), can be indexed to the tetragonal phase of  $\text{FeTe}_{1-x}\text{Se}_x$ , showing the phase purity when the ratio of Se is below 0.7. Figure 2b presents the enlarged segments of the (001) reflections. When  $x$  in  $\text{FeTe}_{1-x}\text{Se}_x$  increases, the (001) peak shifts to larger  $2\theta$  values, which is consistent with the fact that the  $c$ -axis length decreases with increasing  $x$ . The full widths at half maximum (FWHM),  $\delta(2\theta)$ , of all the samples are in the range of  $0.14^\circ$  and  $0.37^\circ$ , demonstrating the uniform compositional distribution of the  $\text{FeTe}_x\text{Se}_{1-x}$  (Figure S3).

To study the structure of  $\text{FeTe}_{1-x}\text{Se}_x$  nanosheets at the atomic scale, high-angle annular dark-field aberration-corrected scanning transmission electron microscopy (HAADF-STEM) was performed. The samples were transferred from the  $\text{SiO}_2/\text{Si}$  substrate to the Cu grid by a poly(methyl methacrylate) (PMMA)-assisted method (see the Experimental Section for details). A typical atomic-resolution HAADF-STEM image of the tetragonal-phase  $\text{FeTe}_{1-x}\text{Se}_x$  is depicted in Figure 3a. Figure 3b shows the enlarged STEM image of Figure 3a. The image contrast in a STEM-ADF image is proportional to the  $Z$  atomic number varying approximately as  $Z^{1.6-1.7}$ .<sup>25,26</sup> From the contrast difference in Figure 3a and 3b, it can be clearly identified that brighter atoms represent Te or Se atoms, while darker atoms represent Fe atoms. Besides, the atomic arrangement in Figure 3b matches well with the structural model viewed from the  $c$  direction in Figure 1b. The corresponding fast Fourier transform (FFT) pattern in Figure



3c reveals a single set of spots with square arrangement, which corresponds to the tetragonal phase along the [001] zone axis. Further, energy-dispersive X-ray spectroscopy (EDX) mapping measurement was performed (Figure 3d-g). The mapping results show the homogeneous distribution of Fe, Se and Te elements throughout the entire nanosheet. The line-scanning measurement was also performed (Figure S5), and the results are consistent with the elemental mapping results. In addition, to visualize the cross-sectional structure of the  $\text{FeTe}_{1-x}\text{Se}_x$  nanosheet, a single  $\text{FeTe}_{1-x}\text{Se}_x$  nanosheet was cut via the focused ion beam (FIB) technique and then characterized by HAADF-STEM (Figure 3h-n). The HAADF-STEM image of the cross section of a  $\text{FeTe}_{1-x}\text{Se}_x$  nanosheet is shown in Figure 3h. The magnified image is shown in Figure 3i. It can be clearly seen that the atomic arrangement matches well with the structural model viewed from the b direction in Figure 1b. The corresponding FFT pattern is illustrated in Figure 3j, corresponding to the tetragonal phase along the [010] zone axis. Homogenous EDX mapping result of Fe, Se and Te elements from the side view further confirms the uniform elemental distribution without phase segregation. EDX results of  $\text{FeTe}_{1-x}\text{Se}_x$  single flake with different compositions are also presented in Figure S6. All these results together suggest that the  $\text{FeTe}_{1-x}\text{Se}_x$  nanosheets prepared by our CVD method have good crystallinity and uniformity.

To further characterize the quality of as-grown  $\text{FeTe}_{1-x}\text{Se}_x$  nanosheets, low-temperature transport experiments were carried out. Figure 4a shows the optical image of the hall bar configuration. A piece of thick BN flake was necessarily capped on the device after

lift-off process to prevent the oxidation of the sample. The temperature dependence of relative longitudinal resistance  $R/R_{T=280K}$  under zero magnetic field is illustrated in Figure 4b. In the previous reports, either metallic or semiconducting behavior can be found in the  $\text{FeTe}_{1-x}\text{Se}_x$  crystals due to the existence of excess interstitial Fe atoms.<sup>24,27</sup> The resistivity of our sample exhibits the metallic behavior, which corresponds to the sample with slightly excess iron atoms.<sup>28</sup> The inset figure in Figure 4b is the zoomed resistance from 1.5 to 15 K. The onset temperature of the superconducting transition ( $T_{\text{onset}}$ ) is 12.4 K. Considering the highest  $T_{\text{onset}}$  for  $\text{FeTe}_{1-x}\text{Se}_x$  crystals is 14.5 K, our result is quite close to that of the crystal.<sup>24</sup> In the low temperature region, an interesting two-step superconducting transition was observed. This may be attributed to the abrupt change in the velocity of dissociated vortex-antivortex (V-AV) pairs or to the transition from the V-AV flow state to the normal regime.<sup>29</sup> The detailed  $I$ - $V$  curve under different temperatures of our  $\text{FeTe}_{1-x}\text{Se}_x$  sample was illustrated in Figure 4c. The presence of zero-resistance plateau further proves the existence of superconducting states, which is consistent with the result shown in Figure 4b. The low temperature transport behavior of our sample under magnetic field was further studied. Figure 4d shows the temperature-dependent  $R/R_{T=280K}$  under out-of-plane ( $H_{\perp}$ ) magnetic field. At the beginning of superconducting transition, the magnetoresistance changes more and more swiftly with the increase of magnetic field, indicating the increasing volume of superconducting islands. However, when the temperature decreases further, the magnetoresistance responds slighter to the magnetic field. This is because the  $\text{FeTe}_{1-x}\text{Se}_x$  has a high upper critical field<sup>30</sup>, such that a small increase in the magnetic field

will not result in an obvious change of the magnetoresistance. Figure 4e shows the temperature-dependent resistance under perpendicular magnetic fields, the magnetic field-dependent feature further confirms the existence of superconductivity. To calculate the upper critical fields for our samples, the extended Werthamer–Helfand–Hohenberg (WHH) model with contributions from Pauli paramagnetic effect is used here,

$$B_{c2}(0) = -0.693 \left( \frac{dB_{c2}}{dT} \right)_{T_c} T_c$$

where  $B_{c2}$  is the upper critical field and  $T_c$  is the critical superconducting transition temperature.<sup>30</sup> Here, we define the critical superconducting transition temperature  $T_c$  under magnetic field by where the resistance is 50% of the normal state value  $R_N$ . Figure 4f shows the  $B_{c2}$  dependence of  $T_c$  of  $\text{FeTe}_{1-x}\text{Se}_x$  samples, which is extracted from Figure 4e. The zero-temperature upper critical field  $B_{c2}(0)$  were found to be corresponding to 31.6 T. Then, the data then were fitted according to the standard Ginzburg–Landau theory:  $B_{c2} = \frac{\Phi_0}{2\pi\xi_{GL}^2} \left( 1 - \frac{T}{T_c} \right)$ , where  $\Phi_0$  is the flux quantum and equal to  $h/2e$  and  $\xi_{GL}$  is the Ginzburg–Landau superconducting coherence length. The  $\xi_{GL}$  derived from the fitting of  $B_{c2}$  is about 3.7 nm at  $T = 0$  K. Further, the  $I$ - $V$  data at different temperature are presented on a double logarithmic scale and shows a clear power-law behavior, corresponding to the BKT transition (Figure S8). Since the BKT transition is a signature of 2D superconductivity, this indicates that the quasi-2D superconductivity exists in our sample although  $\xi_{GL}$  is smaller than the thickness of our sample. In addition, a strong zero bias conductance peak (ZBCP) is observed when the  $dI/dV$  vs bias voltage is plotted (Figure S8), which could possibly be the evidence for

the helical hinge state of  $\text{FeTe}_{1-x}\text{Se}_x$ .<sup>31</sup> The presence of the ZBCP indicates the possibility to observe topological superconductivity in our sample, which deserves further study in future.

It was found that the usage of mixed iron precursor is critical to obtain high-quality superconducting  $\text{FeTe}_{1-x}\text{Se}_x$  nanosheets. If only  $\text{FeCl}_2$  was used as iron precursor, the zero-resistance state will not be achieved (Figure S9). In addition, the  $I$ - $V$  sweep shows a step-like feature and clear hysteresis, indicating the formation of underdamped Josephson junction.<sup>32,33</sup> This is due to the imperfection of prepared sample, which contains defects that can only support a smaller critical current. To further understand this phenomenon, the  $\text{FeTe}_{1-x}\text{Se}_x$  samples prepared by using  $\text{FeCl}_2$  and  $\text{Fe}_2\text{O}_3/\text{FeCl}_2$ , respectively, are both examined by X-ray photoelectron spectroscopy (XPS). Both survey scanning XPS spectra for  $\text{FeTe}_{1-x}\text{Se}_x$  confirm the presence of Fe, Se, and Te elements (Figure S10). However, in the sample prepared by using  $\text{FeCl}_2$  as the iron precursor, an obvious Cl 2p peak is observed (Figure S12), while no Cl 2p peak can be observed in the sample prepared by using  $\text{Fe}_2\text{O}_3/\text{FeCl}_2$  as the iron precursor (Figure S11). Due to the volatile nature of  $\text{FeCl}_2$ , the vapor pressure of  $\text{FeCl}_2$  is difficult to be controlled at the reaction temperature, resulting in a considerable doping of  $\text{Cl}^-$  in the sample when  $\text{FeCl}_2$  is used as precursor. The existence of  $\text{Cl}^-$  may degrade the local superconductivity of our material, and results in localized weak spots.<sup>34</sup> In contrast, by mixing  $\text{Fe}_2\text{O}_3$  and  $\text{FeCl}_2$  as precursor, the residue  $\text{Cl}^-$  in the sample was largely reduced. This could be due to the inhibitor effect of the  $\text{Fe}_2\text{O}_3$ .<sup>35</sup> Both  $\text{Fe}_2\text{O}_3$  and its reduction

product  $\text{Fe}_3\text{O}_4$  have high melting points, and the existence of a large amount of these oxides can act as physical filter for the  $\text{FeCl}_2$  vapor at the reaction temperature. This guarantees the stable release of  $\text{FeCl}_2$  and enables the fully depletion of  $\text{Cl}^-$  on the substrate, thus high-quality sample could be obtained. The relative small superconducting coherence length of  $\text{FeTe}_{1-x}\text{Se}_x$  makes its superconductivity rather sensitive to the defects in the material.<sup>36</sup> This can also be a platform to evaluate different synthetic strategies by low-temperature transport measurement and give us insight on how to prepare high quality superconducting nanomaterials.

## Conclusion

We used an atmosphere-pressure CVD approach to grow  $\text{FeTe}_{1-x}\text{Se}_x$  nanosheets on various substrates, including  $\text{SiO}_2/\text{Si}$ ,  $\text{Si}(100)$  and  $\text{STO}(110)$ . Our method enables both thickness and composition control of  $\text{FeTe}_{1-x}\text{Se}_x$  nanosheets, thus offers a facile option for the growth of this promising topological superconductor in addition to MBE and PLD, which are usually costly and time-consuming. Hopefully, we believe our method could accelerate the research in discovering the fascinating properties of  $\text{FeTe}_{1-x}\text{Se}_x$ . In addition, our low-temperature transport measurement was performed on  $\text{FeTe}_{1-x}\text{Se}_x$  nanosheets grown on amorphous  $\text{Si}/\text{SiO}_2$ . This helps to study the intrinsic low-temperature property of this material because of the absence of strain induced by the growth substrate. This could also be extended to study the substrate-dependent superconducting property of  $\text{FeTe}_{1-x}\text{Se}_x$  nanosheets in future. Most importantly, our work provides a new synthetic strategy for the growth of high-quality iron-based

superconductors by mixing  $\text{Fe}_2\text{O}_3$  and  $\text{FeCl}_2$  as the iron precursors. We believe this strategy can be extended to grow other 2D materials and would benefit the development of the current solid precursor-based CVD technique.

## Experimental Section

Chemical vapor deposition of ultrathin  $\text{FeTe}_{1-x}\text{Se}_x$  nanosheets:

All chemicals are purchased from Sigma and used without purification. Ambient pressure CVD growth of  $\text{FeTe}_{1-x}\text{Se}_x$  nanosheets were conducted in a 1-inch outer diameter fused quartz tube heated by a single zone (Thermcraft Protégé XST) split tube furnace. A mixture of  $\text{Fe}_2\text{O}_3$  and  $\text{FeCl}_2$  powders (10 mg,  $\text{Fe}_2\text{O}_3:\text{FeCl}_2=5:1$ ) were placed in an alumina boat located in the center of the furnace. 285 nm  $\text{SiO}_2/\text{Si}$  or other substrates was placed facing down at the downstream. Selenium powder (200 mg) and tellurium powder (500 mg) were placed at the upstream of the quartz tube, and the ratio between Te and Se were tuned by controlling the temperature of Te and Se. 80 sccm (cubic centimeters per minute) Ar and 6 sccm  $\text{H}_2$  were used as carrier gases. The furnace was heated to a temperature range between 500 to 540 °C in 15 min and kept at the reaction temperature for 5 mins to allow the synthesis of  $\text{FeTe}_{1-x}\text{Se}_x$  nanosheets. After that, the furnace was naturally cooled to room temperature by opening the furnace without changing the flow rates of carrier gases.

Device fabrication and transport measurements:

A  $\text{Si}/\text{SiO}_2$  substrate was used to deposit the  $\text{FeTe}_{1-x}\text{Se}_x$  nanosheets directly to avoid an

additional transfer process for transport measurements. Standard e-beam lithography (EBL) was used to fabricate Hall-bar devices. Next, Cr/Au electrodes with a thickness of 5/80 nm were deposited on the sample using an electron-beam evaporator. After the lift-off process in acetone, the  $\text{FeTe}_{1-x}\text{Se}_x$ -based devices were obtained. The electrical contacts were made by wire bonding Al wires onto the six electrodes on a Hall-bar structure. Transport experiments were performed in an Oxford cryostat with the temperature ranging from 280 to 1.5 K and the magnetic field up to 8 T. The sample resistance and Hall effect were measured by Keithley 6221 triggered with Keithley 2182 with the 21 Hz frequency.

#### Sample characterization:

The as-obtained  $\text{FeTe}_{1-x}\text{Se}_x$  nanosheets were further characterized by optical microscopy (Olympus BX53M). XPS measurements were carried out on the Kratos AXIS Supra system, and the binding energies were calibrated with C 1s binding energy of 284.8 eV. AFM images were taken using the Asylum Research Cypher AFM in tapping mode. ADF-STEM imaging was conducted on an aberration-corrected JEOL ARM-200F equipped with a cold field emission gun, operating at 80 kV, and an Advanced STEM Corrector (ASCOR) probe corrector.

- 1 Hsu, F.-C. *et al.* Superconductivity in the PbO-type structure  $\alpha$ -FeSe. *Proceedings of the National Academy of Sciences* **105**, 14262-14264, doi:10.1073/pnas.0807325105 (2008).
- 2 Song, C.-L. *et al.* Direct Observation of Nodes and Twofold Symmetry in FeSe Superconductor. *Science* **332**, 1410-1413, doi:10.1126/science.1202226 (2011).
- 3 Mizuguchi, Y., Tomioka, F., Tsuda, S., Yamaguchi, T. & Takano, Y. Superconductivity at 27K in tetragonal FeSe under high pressure. *Applied Physics Letters* **93**, 152505, doi:10.1063/1.3000616 (2008).
- 4 Baek, S. H. *et al.* Orbital-driven nematicity in FeSe. *Nature Materials* **14**, 210-214, doi:10.1038/nmat4138 (2015).
- 5 Wang, Q.-Y. *et al.* Interface-Induced High-Temperature Superconductivity in Single Unit-Cell FeSe Films on SrTiO<sub>3</sub>. *Chinese Physics Letters* **29**, 037402, doi:10.1088/0256-307x/29/3/037402 (2012).
- 6 Ge, J.-F. *et al.* Superconductivity above 100 K in single-layer FeSe films on doped SrTiO<sub>3</sub>. *Nature Materials* **14**, 285-289, doi:10.1038/nmat4153 (2015).
- 7 Hao, N. & Hu, J. Topological quantum states of matter in iron-based superconductors: from concept to material realization. *National Science Review* **6**, 213-226, doi:10.1093/nsr/nwy142 (2018).
- 8 Wu, X., Qin, S., Liang, Y., Fan, H. & Hu, J. Topological characters in  $\text{Fe}(\text{Te})_{1-x}\text{Se}_x$  thin films. *Physical Review B* **93**, 115129, doi:10.1103/PhysRevB.93.115129 (2016).
- 9 Wang, Z. *et al.* Topological nature of the  $\text{FeSe}_{0.5}\text{Te}_{0.5}$  superconductor. *Physical Review B* **92**, 115119, doi:10.1103/PhysRevB.92.115119 (2015).
- 10 Hanaguri, T., Niitaka, S., Kuroki, K. & Takagi, H. Unconventional  $d$ -Wave Superconductivity in Fe(Se,Te). *Science* **328**, 474-476, doi:10.1126/science.1187399 (2010).
- 11 Wang, D. *et al.* Evidence for Majorana bound states in an iron-based superconductor. *Science* **362**, 333-335, doi:10.1126/science.aao1797 (2018).
- 12 Zhu, S. *et al.* Nearly quantized conductance plateau of vortex zero mode in an iron-based superconductor. *Science* **367**, 189-192, doi:10.1126/science.aax0274 (2020).
- 13 Zhang, P. *et al.* Observation of topological superconductivity on the surface of an iron-based superconductor. *Science* **360**, 182-186, doi:10.1126/science.aan4596 (2018).
- 14 Shi, X. *et al.* FeTe<sub>1-x</sub>Se<sub>x</sub> monolayer films: towards the realization of high-temperature connate topological superconductivity. *Science Bulletin* **62**, 503-507, doi:<https://doi.org/10.1016/j.scib.2017.03.010> (2017).
- 15 Mele, P. Superconducting properties of iron chalcogenide thin films. *Science and Technology of Advanced Materials* **13**, 054301, doi:10.1088/1468-6996/13/5/054301 (2012).
- 16 Song, Q. *et al.* Evidence of cooperative effect on the enhanced superconducting transition temperature at the FeSe/SrTiO<sub>3</sub> interface. *Nature Communications* **10**,



- 758, doi:10.1038/s41467-019-08560-z (2019).
- 17 Deng, Y. *et al.* Controlled Growth of 3R Phase Tantalum Diselenide and Its Enhanced Superconductivity. *Journal of the American Chemical Society* **142**, 2948-2955, doi:10.1021/jacs.9b11673 (2020).
  - 18 Cai, Z., Liu, B., Zou, X. & Cheng, H.-M. Chemical Vapor Deposition Growth and Applications of Two-Dimensional Materials and Their Heterostructures. *Chemical Reviews* **118**, 6091-6133, doi:10.1021/acs.chemrev.7b00536 (2018).
  - 19 Zhou, J. *et al.* A library of atomically thin metal chalcogenides. *Nature* **556**, 355-359, doi:10.1038/s41586-018-0008-3 (2018).
  - 20 Li, J. *et al.* General synthesis of two-dimensional van der Waals heterostructure arrays. *Nature* **579**, 368-374, doi:10.1038/s41586-020-2098-y (2020).
  - 21 Zhang, Z. *et al.* Robust epitaxial growth of two-dimensional heterostructures, multiheterostructures, and superlattices. *Science* **357**, 788-792, doi:10.1126/science.aan6814 (2017).
  - 22 Kang, L. *et al.* Phase-controllable growth of ultrathin 2D magnetic FeTe crystals. *arXiv preprint arXiv:1912.06364* (2019).
  - 23 Tang, F. *et al.* Quasi-2D superconductivity in FeTe<sub>0.55</sub>Se<sub>0.45</sub> ultrathin film. *Journal of Physics: Condensed Matter* **31**, 265702, doi:10.1088/1361-648x/ab14c3 (2019).
  - 24 Dong, C. *et al.* Revised phase diagram for the FeTe<sub>1-x</sub>Se<sub>x</sub> system with fewer excess Fe atoms. *Physical Review B* **84**, 224506, doi:10.1103/PhysRevB.84.224506 (2011).
  - 25 Krivanek, O. L. *et al.* Atom-by-atom structural and chemical analysis by annular dark-field electron microscopy. *Nature* **464**, 571-574, doi:10.1038/nature08879 (2010).
  - 26 Zhao, X., Ning, S., Fu, W., Pennycook, S. J. & Loh, K. P. Differentiating Polymorphs in Molybdenum Disulfide via Electron Microscopy. *Advanced Materials* **30**, 1802397, doi:<https://doi.org/10.1002/adma.201802397> (2018).
  - 27 Liu, T. J. *et al.* Charge-carrier localization induced by excess Fe in the superconductor Fe<sub>1+y</sub>Te<sub>x</sub>Se<sub>x</sub>. *Physical Review B* **80**, 174509, doi:10.1103/PhysRevB.80.174509 (2009).
  - 28 Sun, Y. *et al.* Multiband effects and possible Dirac fermions in Fe<sub>1+y</sub>Te<sub>0.6</sub>Se<sub>0.4</sub>. *Physical Review B* **89**, 144512, doi:10.1103/PhysRevB.89.144512 (2014).
  - 29 Saito, Y., Itahashi, Y. M., Nojima, T. & Iwasa, Y. Dynamical vortex phase diagram of two-dimensional superconductivity in gated MoS<sub>2</sub>. *Physical Review Materials* **4**, 074003, doi:10.1103/PhysRevMaterials.4.074003 (2020).
  - 30 Khim, S. *et al.* Evidence for dominant Pauli paramagnetic effect in the upper critical field of single-crystalline FeTe<sub>0.6</sub>Se<sub>0.4</sub>. *Physical Review B* **81**, 184511, doi:10.1103/PhysRevB.81.184511 (2010).
  - 31 Gray, M. J. *et al.* Evidence for Helical Hinge Zero Modes in an Fe-Based Superconductor. *Nano Letters* **19**, 4890-4896,

- doi:10.1021/acs.nanolett.9b00844 (2019).
- 32 Zhang, E. *et al.* Signature of quantum Griffiths singularity state in a layered quasi-one-dimensional superconductor. *Nature Communications* **9**, 4656, doi:10.1038/s41467-018-07123-y (2018).
- 33 Yu, W. & Stroud, D. Resistance steps in underdamped Josephson-junction arrays. *Physical Review B* **46**, 14005-14009, doi:10.1103/PhysRevB.46.14005 (1992).
- 34 Telford, E. J. *et al.* Doping-Induced Superconductivity in the van der Waals Superatomic Crystal Re<sub>6</sub>Se<sub>8</sub>Cl<sub>2</sub>. *Nano Letters* **20**, 1718-1724, doi:10.1021/acs.nanolett.9b04891 (2020).
- 35 Shi, R. *et al.* Oxide Inhibitor-Assisted Growth of Single-Layer Molybdenum Dichalcogenides (MoX<sub>2</sub>, X = S, Se, Te) with Controllable Molybdenum Release. *ACS Nano* **14**, 7593-7601, doi:10.1021/acsnano.0c03469 (2020).
- 36 Putti, M. *et al.* New Fe-based superconductors: properties relevant for applications. *Superconductor Science and Technology* **23**, 034003, doi:10.1088/0953-2048/23/3/034003 (2010).

## Acknowledgments

Z.L. acknowledges the support from National Research Foundation Singapore programme NRF-CRP21-2018-0007 and NRF-CRP22-2019-0007, Singapore Ministry of Education via AcRF Tier 3 Programme 'Geometrical Quantum Materials' (MOE2018-T3-1-002), AcRF Tier 2 (MOE2016-T2-1-131) and AcRF Tier 1 RG4/17 and RG7/18. This research is also supported by A\*STAR under its AME IRG Grant (Project No. 19283074).

## Author contributions

Z.L. and X.R.W. conceived and supervised the project. D.H., C.Y., X.W., X.Z. and L.K. designed the experiments. D.H., J.L. and L.K. synthesized and characterized the sample. D.H. and X.W. fabricated the devices. C.Y. and X.W. carried out the transport measurements and analyzed the results. J.L., X.Z. and S.J.P. did the HRTEM and STEM

measurement and data analysis. All the authors discussed the results and commented on the manuscript.

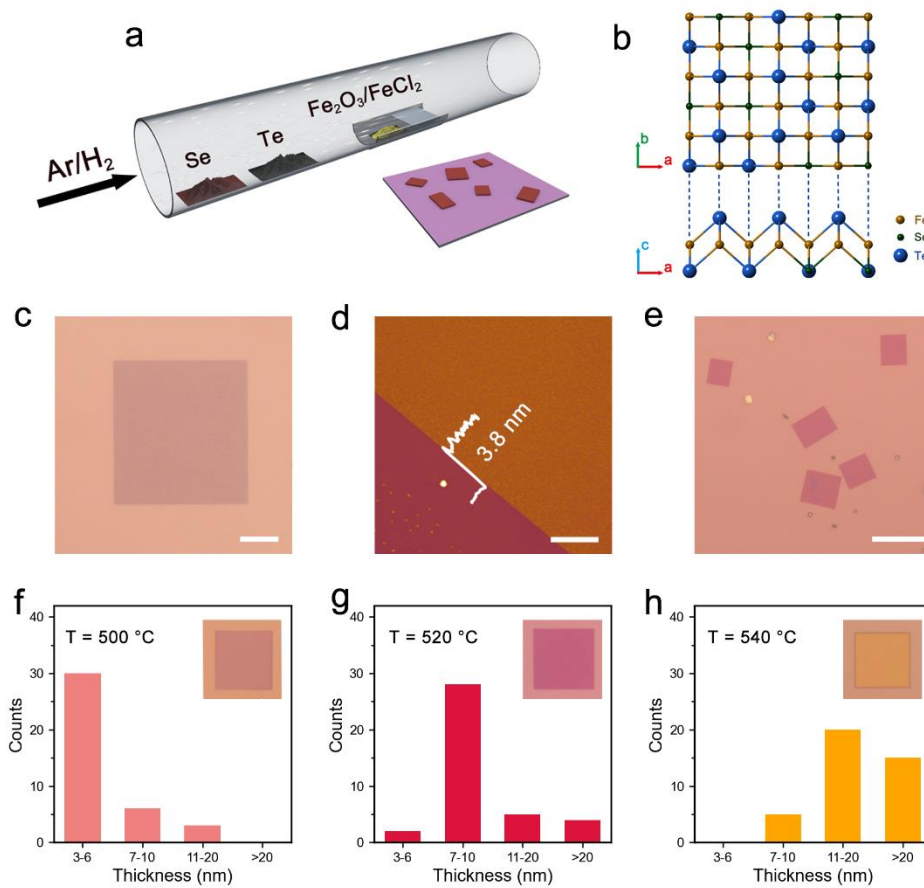


**Figure 1.** Structural characterization of  $\text{FeTe}_{1-x}\text{Se}_x$  nanosheets. **(a)** Experimental setup of the CVD method. **(b)** Model of tetragonal  $\text{FeTe}_{1-x}\text{Se}_x$  viewed from two different directions, i.e., c and b directions. **(c)** OM image of a typical ultrathin  $\text{FeTe}_{1-x}\text{Se}_x$  nanosheet. **(d)** AFM image of the ultrathin  $\text{FeTe}_{1-x}\text{Se}_x$  nanosheet with thickness of 3.8 nm. **(e)** Low-magnification OM image of uniform  $\text{FeTe}_{1-x}\text{Se}_x$  nanosheets on the  $\text{SiO}_2/\text{Si}$  substrate. **(f-h)** Statistic thickness distributions and representative OM images (insets) of  $\text{FeTe}_{1-x}\text{Se}_x$  nanosheets synthesized under reaction temperatures of **(f)** 500 °C, **(g)** 520 °C and **(h)** 540 °C, respectively. Scale bars, **(c)** 10  $\mu\text{m}$ ; **(d)** 1  $\mu\text{m}$ ; **(e)** 20  $\mu\text{m}$ .

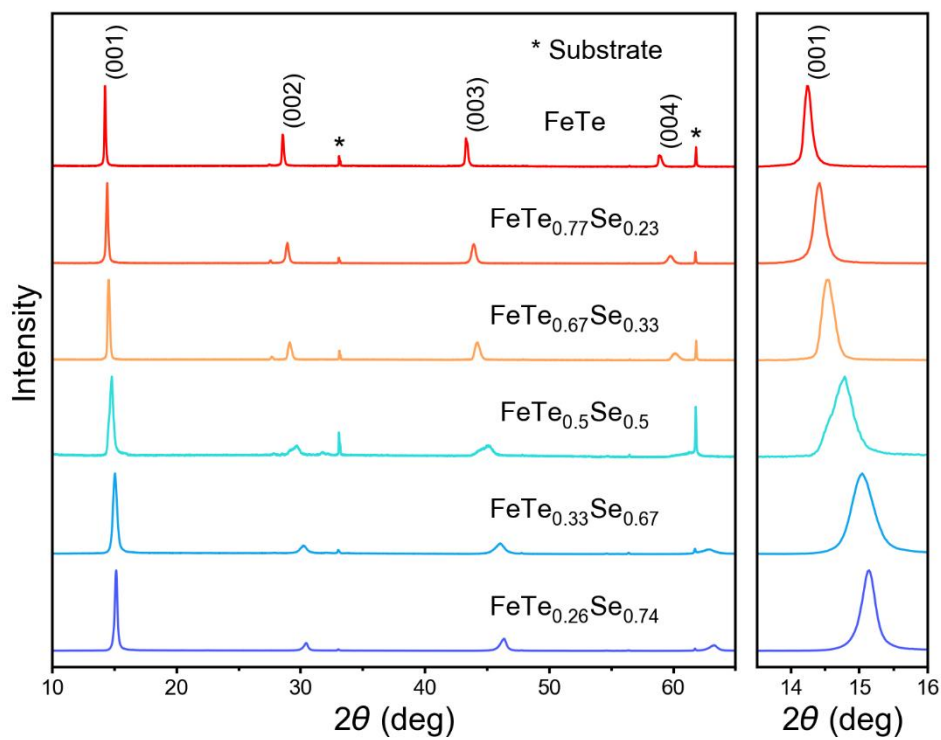


**Figure 2.** XRD patterns of **(a)**  $\text{FeTe}_{1-x}\text{Se}_x$  with different compositions and **(b)** the enlarged segments of the (001) peak.

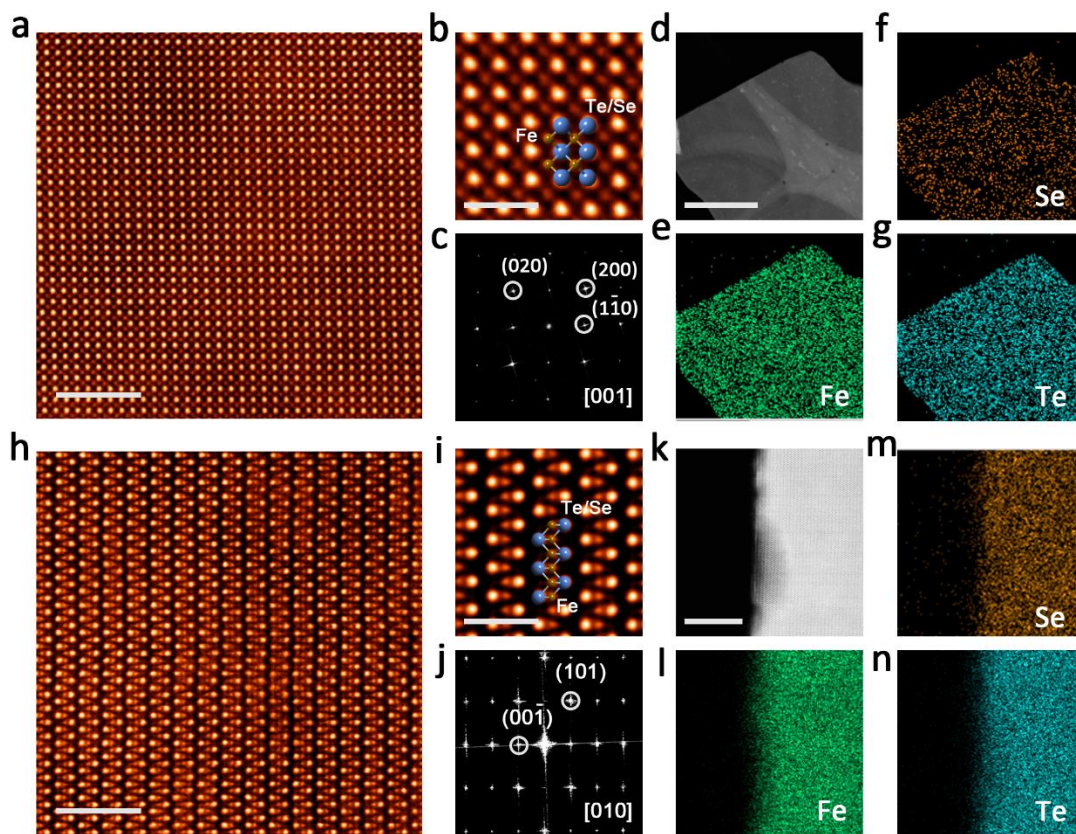


**Figure 3.** STEM characterizations of  $\text{FeTe}_{1-x}\text{Se}_x$  nanosheets. **(a)** HAADF-STEM image of the  $\text{FeTe}_{1-x}\text{Se}_x$  viewed along the  $c$  axis. **(b)** The enlarged HAADF-STEM image from the dotted square in **(a)**. **(c)** FFT pattern taken from **(b)**, showing its single crystal nature. **(d)** HAADF-STEM image of a  $\text{FeTe}_{1-x}\text{Se}_x$  nanosheet and the corresponding elemental mappings of **(e)** Fe, **(f)** Se and **(g)** Te, **(h)** HAADF-STEM image of the cross section of the  $\text{FeTe}_{1-x}\text{Se}_x$  nanosheet. **(i)** The enlarged HAADF-STEM image from the dotted square in **(h)**. **(j)** FFT pattern taken from **(i)**, showing its single crystal nature. **(k)** Cross-sectional HAADF-STEM image of a  $\text{FeTe}_{1-x}\text{Se}_x$  flake and the corresponding elemental mappings of **(l)** Fe, **(m)** Se and **(n)** Te. Scale bars: **(a, h)** 2 nm; **(b, i)** 1 nm; **(d)**, 250 nm; **(k)** 10 nm.

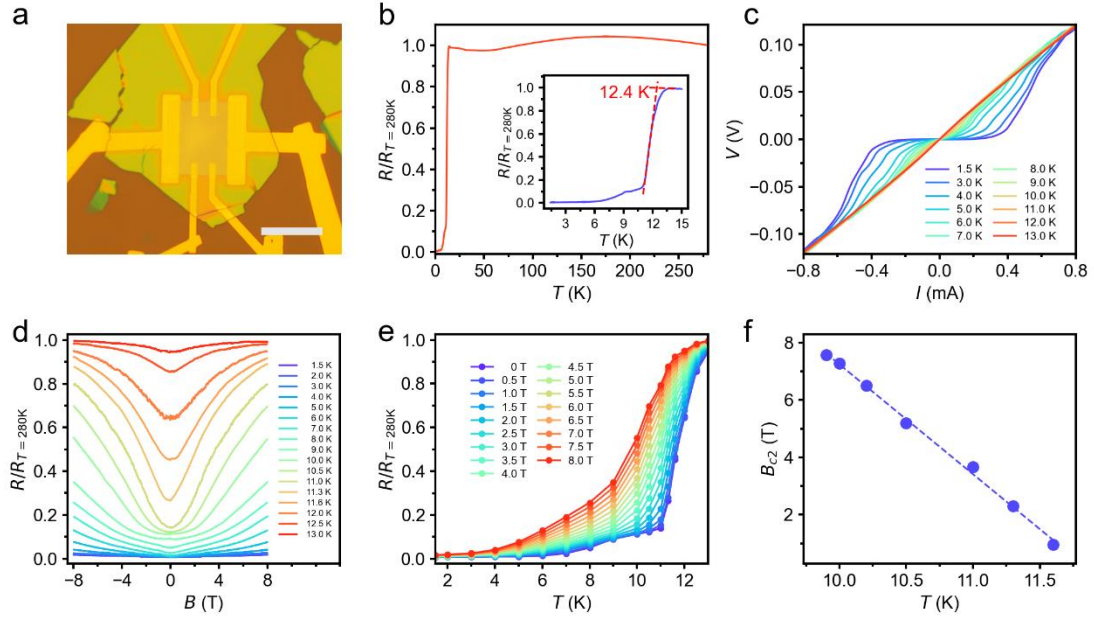


**Figure 4.** Low-temperature transport properties of synthesized  $\text{FeTe}_{1-x}\text{Se}_x$  nanoflake. **(a)** The optical image of the measured device. Scale bar, 20  $\mu\text{m}$ ; **(b)** Temperature dependence of relative longitudinal resistance  $R/R_{T=280\text{K}}$ , the inset is the enlarged region; **(c)**  $I$ - $V$  curves under zero magnetic fields; **(d)** Magnetoresistance of the device measured at different temperature under perpendicular magnetic field; **(e)** Temperature-dependent  $R/R_{T=280\text{K}}$  measured under perpendicular magnetic fields; **(f)** Upper critical field ( $B_{c2}$ ) as a function of temperature. The solid line is the linear fit to the data.